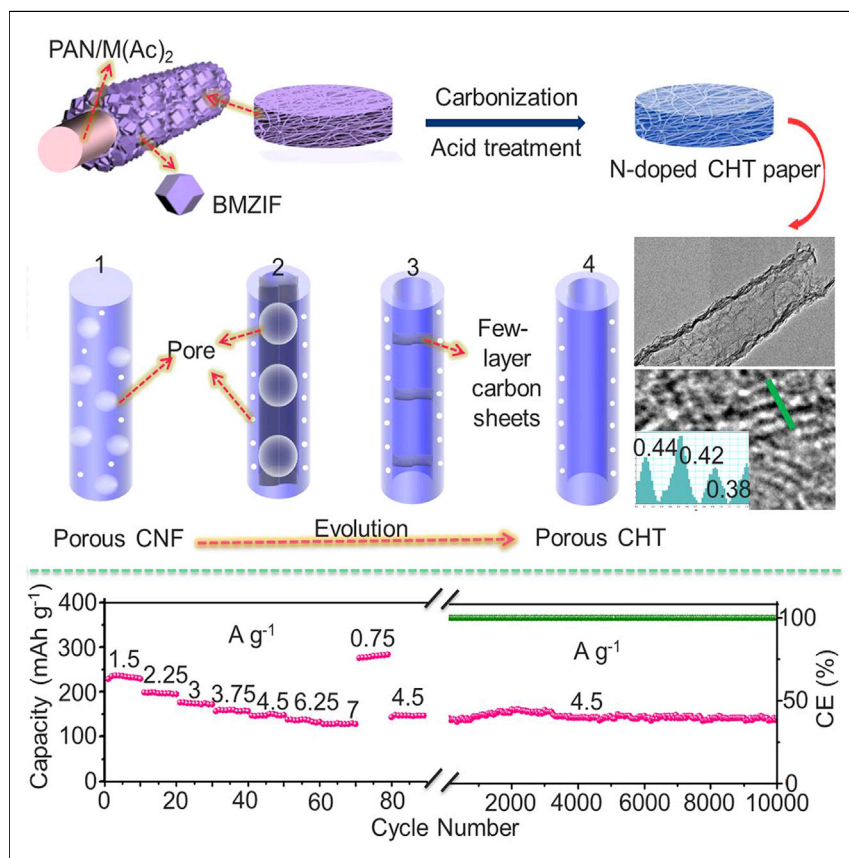


Article

Nitrogen-Doped Carbon for Sodium-Ion Battery Anode by Self-Etching and Graphitization of Bimetallic MOF-Based Composite



N-doped porous carbon with the large interlayer spacing needed for Na⁺ intercalation is synthesized by a method of self-etching and graphitization of bimetallic MOF-based composites and shows good electrochemical performance for Na-ion batteries.

Yuming Chen, Xiaoyan Li,
Kyusung Park, ..., Haitao Huang,
Ju Li, John B. Goodenough

aphhuang@polyu.edu.hk (H.H.)
liju@mit.edu (J.L.)
jgoodenough@mail.utexas.edu (J.B.G.)

HIGHLIGHTS

Bimetallic MOF-based
nanocomposites enable self-
etching and graphitization

A N-doped porous carbon tubule
possesses large interlayer spacing
up to 0.44 nm

The carbon tubule paper
manifests ultralong cycling life for
Na-ion batteries

Article

Nitrogen-Doped Carbon for Sodium-Ion Battery Anode by Self-Etching and Graphitization of Bimetallic MOF-Based Composite

Yuming Chen,^{1,2,3,4,6} Xiaoyan Li,^{1,6} Kyusung Park,² Wei Lu,⁵ Chao Wang,^{3,4} Weijiang Xue,^{3,4} Fei Yang,^{3,4} Jiang Zhou,^{3,4} Liumin Suo,^{3,4} Tianquan Lin,^{3,4} Haitao Huang,^{1,*} Ju Li,^{3,4,7,*} and John B. Goodenough^{2,*}

SUMMARY

The greater availability of sodium (Na) over lithium (Li) motivates development of a Na-ion battery that can compete with a Li-ion battery. In these batteries, both electrodes consist of hosts into which Li^+ or Na^+ can be inserted reversibly. Graphite has been the anode host for Li-ion batteries, but the Na^+ ion is too large to be inserted easily between the flat graphene layers of common graphite. We report the synthesis and electrochemical performance of N-doped carbon nanofibers and tubules with an organic-liquid electrolyte and a large fraction of graphitic carbon and larger spacing (0.38–0.44 nm) between carbon sheets; the carbon hollow tubules yield ultrastable (10,000 cycles), high-rate capabilities of Na^+ intercalation and deintercalation with reversible capacities up to 346 mAh g⁻¹.

INTRODUCTION

Lithium-ion batteries (LIBs) open up huge potential markets for rechargeable batteries in powering vehicles and storing electric power for the grid.^{1–5} However, lithium (Li) is a limited resource that, like oil, is unevenly distributed globally.^{6–8} Sodium (Na), on the other hand, is readily available from the ocean, so Na-ion batteries (SIBs) could one day provide strategic alternatives.^{9–13} Like LIBs, SIBs would have an organic-liquid solvent-based electrolyte and electrode hosts into which the working cation, Na^+ , would be reversibly inserted.^{14,15} However, the larger size of the Na^+ ion challenges the potential host structures. For example, various forms of graphite have been used as the anode of a LIB, but the spacing between the layers is too small to accept Na^+ ions. Here, we report the scalable synthesis of a nitrogen-doped porous carbon with large graphitic fractions with spacing sufficient for insertion of Na^+ at high rates. Carbon nanofibers (CNFs) and carbon nanotubes (CNTs) are being developed as high-capacity anodes for LIBs, but they provide poor performance as anodes for SIBs^{7,16} because the spacing is too narrow.¹⁷ Theoretical calculations indicate that the minimum layer separation for facile Na^+ motion is 0.37 nm.¹⁶ One strategy to enhance the capacity of Na^+ insertion is the development of void, vacancy, and curved graphene defects in the CNF or CNT anode.^{18–24} A second approach has been to expand the separation of the layers through an oxidation process or thermal treatment.^{16,25} A third approach has been heteroatom doping to enhance the ionic conductivity and surface hydrophilicity.^{26–31}

In this work, we synthesized N-doped carbon hollow tubules (CHTs) with heteroatom doping and a large fraction of sp^2 carbon with the larger interlayer spacing needed for Na^+ intercalation by a method of self-etching and graphitization of bimetallic metal-organic-framework (MOF)-based nanocomposites.

The Bigger Picture

Carbon nanofibers (CNFs) and carbon hollow tubules (CHTs) are attractive anode materials for Na-ion batteries. Here, we report a method of self-etching and graphitization of metal-organic-framework-based nanocomposites for synthesizing a series of N-doped porous nanocarbons with a large fraction of graphitic carbon with larger spacing (0.38–0.44 nm). The N-doped porous CHT paper shows an outstanding cycling life over 10,000 cycles with no clear decline in capacity. Such a strategy could provide new avenues for the rational engineering of nanostructured N-doped carbonaceous materials with large graphene interlayer spacing for better Na-ion batteries.

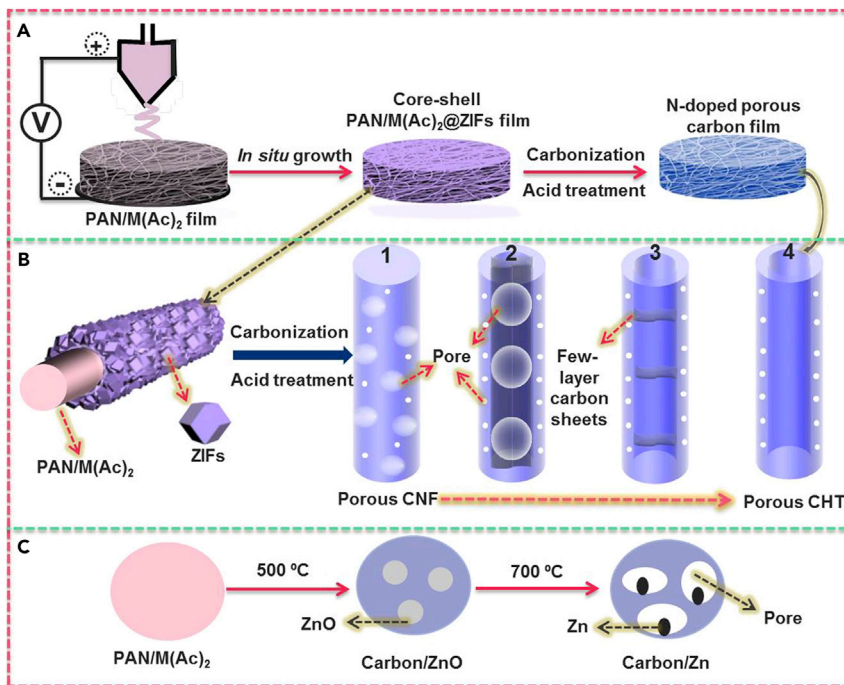


Figure 1. Schematic Illustration of the Synthesis of a Series of 1D Nanocarbons from Porous N-Doped CNFs to CHTs with Enlarged Graphene Interlayer Spacing

(A) The synthesis process of the 1D carbons.

(B) Evolution of porous CNFs to CHTs.

(C) Formation process of the porous carbon core.

See also Figures S1 and S2.

RESULTS

Figure 1 provides a schematic illustration of a route for the synthesis of N-doped, porous CHTs with a large fraction of graphitization with sufficient spacing (0.38–0.44 nm) for Na⁺ intercalation. First, polyacrylonitrile (PAN) was dissolved in dimethyl formate (DMF; Aldrich) solvent. Then variable ratios of zinc acetate Zn(Ac)₂ and cobalt acetate Co(Ac)₂ were uniformly mixed with the PAN solution mentioned above to obtain a homogeneous electrospinning solution. The PAN/Zn(Ac)₂/Co(Ac)₂ composite nanofibers can be easily produced by a simple electrospinning technique, forming a free-standing paper.

Next, the composite nanofiber paper was introduced into ethanol solution containing 2-methyl-imidazole; after 12 hr at room temperature, the potent coordination of 2-methylimidazole to both Zn²⁺ and Co²⁺ ions^{32–34} creates a layer of bimetallic imidazole framework (BMZIF; ZIF stands for zeolitic imidazolate framework, a class of MOFs) coating the composite nanofibers. This reaction is kinetically self-limiting; after a while, both 2-methylimidazole in ethanol solution and metal acetates inside the core of the composite nanofibers are not able to diffuse through the newly formed BMZIF layer for further chemical reaction, giving rise to the PAN/Zn(Ac)₂/Co(Ac)₂@BMZIF core-shell composite structure (Figure 1B).

Upon heating the film to 700°C, the BMZIF coating was carbonized; ZIF-8 (zinc coordinated by four imidazolate rings) enables high N doping of a porous carbon structure,³⁴ and ZIF-67 (cobalt coordinated by four imidazolate rings) provides well-graphitized carbon.^{26,35} Inheriting the advantages of carbons from both ZIF-67

¹Department of Applied Physics, Hong Kong Polytechnic University, Hong Kong, China

²Texas Materials Institute and Materials Science and Engineering Program, University of Texas at Austin, Austin, TX 78712, USA

³Department of Nuclear Science and Engineering, Massachusetts Institute of Technology, Cambridge, MA 02139, USA

⁴Department of Materials Science and Engineering, Massachusetts Institute of Technology, Cambridge, MA 02139, USA

⁵University Research Facility in Materials Characterization and Device Fabrication, Hong Kong Polytechnic University, Hong Kong, China

⁶These authors contributed equally

⁷Lead Contact

*Correspondence:
aphhuang@polyu.edu.hk (H.H.),
liju@mit.edu (J.L.),
jgoodenough@mail.utexas.edu (J.B.G.)

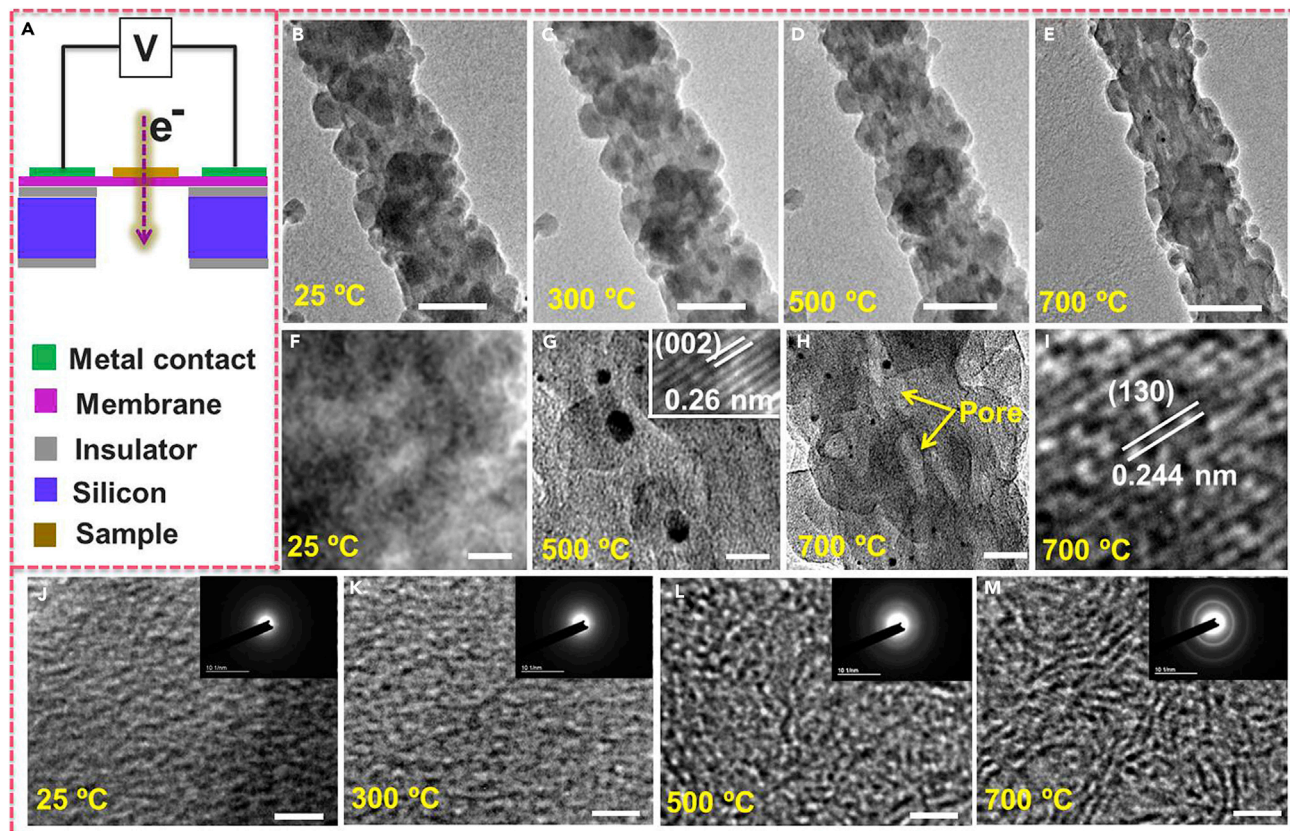
<http://dx.doi.org/10.1016/j.chempr.2017.05.021>

and ZIF-8, the BMZIF layer was converted into N-doped porous carbon with high graphitization. The PAN core was turned into carbon that can be etched by ZnO from the decomposition product of Zn(Ac)₂ in the composite fiber core,^{36,37} as shown in [Figure 1C](#), according to the carbothermal reduction $ZnO + C \rightarrow Zn + CO_2$ or CO. The carbon core can be completely etched out by increasing the content of Zn(Ac)₂.

The free-standing paper was then treated with acid (HCl) to remove the residual metals within the material to yield a N-doped CHT with spacing of 0.38–0.44 nm between the graphene layers ([Figure 1B1–4](#)). The thickness of this free-standing CHT paper is ~70–80 μm and the nominal density is ~0.45 g cm⁻³. The in-plane sheet resistance is ~3 Ohm/sq from four-probe measurements. The paper also possesses good mechanical integrity on bending, which could be useful for making flexible batteries. The as-synthesized free-standing N-doped porous CHT paper exhibits excellent electrochemical performance with high specific capacity, a remarkable rate capability, and a long cycle life of over 10,000 cycles when evaluated as the anode of a SIB with a liquid electrolyte.

Typical field-emission scanning electron microscopy (FESEM) images show that the BMZIFs are grown onto the composite nanofibers ([Figures S1A](#) and [S1B](#)). A core-shell structure can be clearly identified by transmission electron microscopy (TEM; [Figures S1C–S1E](#)). Energy-dispersive X-ray mappings (EDX) show that C, N, Zn, and Co are uniformly distributed throughout the prepared materials ([Figures S1F–S1J](#)), whereas O from the metal acetate is located only in the core of the composite ([Figure S1K](#)), consistent with a PAN/Zn(Ac)₂/Co(Ac)₂ core with a shell of BMZIF. The X-ray diffraction (XRD) pattern of the synthesized hybrids indicates typical diffraction peaks in the ZIF phase ([Figure S2A](#)).^{33,34,38–40}

A heating stage within TEM was used to monitor dynamically the formation of porous CNFs; the temperature was varied from 25°C to 700°C ([Figure 2A](#)). At 300°C, the sample was found to be almost identical to the original ([Figures 2B](#) and [2C](#)). Some black nanoparticles were observed in the composite nanofibers after heating at 500°C ([Figures 2D](#) and [2G](#)). High-resolution TEM (HRTEM) analysis of these particles (inset of [Figure 2G](#)) demonstrated that they have an interplanar distance of 0.26 nm, corresponding well to that of the ZnO (002) plane,⁴¹ indicating that the Zn(Ac)₂ was converted into ZnO nanoparticles during the heating process. These ZnO nanoparticles are only localized in the fiber core, because of the initial distribution of O. TEM and EDX mapping further prove that ZnO/carbon composite nanofibers can be achieved by calcination of PAN/Zn(Ac)₂/Co(Ac)₂ composite nanofibers in inert gas at 500°C ([Figure S3](#)). All the diffraction peaks in the XRD pattern can be well indexed to hexagonal ZnO (JCPDS card no. 36-1451). No peak for the Co-based materials can be observed because of its low content in the composite. Interestingly, some pores can be clearly identified in the CNFs at 700°C ([Figures 2E](#) and [2H](#)), formed by the reaction $ZnO + C \rightarrow Zn + CO_2 \uparrow$ or $CO \uparrow$. Some of the Zn materials formed are evaporated and some can react with Co metal from the decomposition of Co(Ac)₂ to form zinc-cobalt metals such as Zn₁₃Co and Zn₃Co.³⁷ Zn₃Co is not stable at high temperature and will decompose into Co and Zn₁₃Co. An interplanar distance of 0.244 nm corresponding to the CoZn₁₃ (130) plane can be seen ([Figure 2I](#)). [Figure S4](#) shows that porous metal/carbon composite nanofibers can be obtained by heating composite nanofibers in inert gas at 700°C. No black particles can be observed inside the carbon particles after carbonization of the BMZIFs. Co and Zn elements can still be detected everywhere ([Figure S5](#)).



Electron-diffraction and HRTEM analysis were also carried out to study the formation process. Figures 2J–2M show the evolution of selected-area electron-diffraction (SAED) patterns and HRTEM images with increasing temperature. From 25°C to 300°C, no diffraction ring was observed, indicating that the precursors are amorphous, consistent with the HRTEM result (Figures 2J and 2K). When the temperature was increased to 500°C, blurred diffraction rings appeared and a 2- or 3-layer-stacked graphene layer (generally curved) was observed on the HRTEM images (Figure 2L). The SAED pattern in the inset of Figure 2L can be well indexed to carbon, indicating the initiation of graphitization at this stage.^{22,42} The diffraction rings became brighter and sharper with further increase in temperature, implying enhanced graphitization as further confirmed by HRTEM (Figure 2M). As a result, porous CNFs with high graphitization can be produced.

The decomposition of Zn(Ac)₂ in the precursor solution to form ZnO plays an important role in the formation of a porous structure, because etching by ZnO leaves porosities. To verify the morphology evolution of the N-doped porous CHTs, electrospinning solutions with different amounts of zinc acetate were prepared (with the content of the other ingredients fixed) and investigated by TEM (Figure 3). As shown in Figure 3A, the resulting material reveals a fibrous structure, containing a few small pores with low content of Zn(Ac)₂. An increasingly hollow structure can

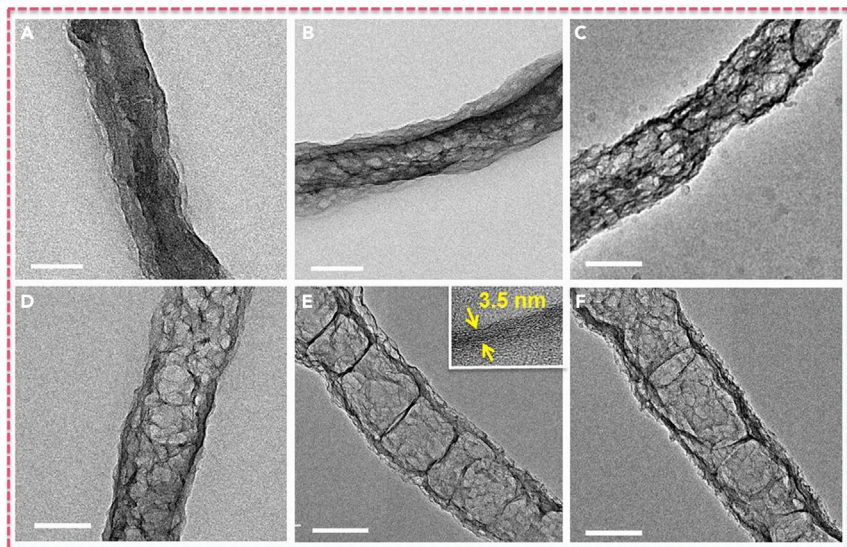


Figure 3. The Evolution of 1D Nanocarbons

TEM images of the evolution of porous CNFs to CHTs wired by few-layer carbon sheets. Scale bars: 100 nm. See also Figure S6.

be identified in Figure 3B as the amount of zinc acetate increases. The morphology of the inner hollow tube can be seen more clearly with an increasing amount of $\text{Zn}(\text{Ac})_2$ in the precursor solution (Figures 3C and 3D). More importantly, when a significant amount of carbon was etched out, CHTs with few carbon nanosheets were formed. The corresponding final materials in Figures 3E and 3F exhibit a bamboo-like structure that is internally wired by segments of carbon layers with a thickness of ~ 3.5 nm. Thus, the porosity of CHTs can be tuned by controlling the content of $\text{Zn}(\text{Ac})_2$ (Figure S6). In addition, the heating temperature also plays an important role in the structure of the final samples. A low calcination temperature is only able to produce porous carbon nanofibers (Figure S7) but not tubules.

Figure 4A shows that the N-doped porous carbon paper has high mechanical flexibility, which could be useful for making flexible batteries. The morphology of the N-doped porous CHTs was characterized by FESEM and HRTEM (Figures 4B–4D). The N-doped porous CHTs show 1D tubular morphology with a length up to several micrometers and a diameter of $\sim 170 \pm 20$ nm (Figure 4B). The hollow tubular structure and rough surface can be observed in Figures 4C and 4D, facilitating the effective transport of ions.⁴³ HRTEM in Figure 4E shows that the d spacing of the carbon sheets in the N-doped porous CHTs is in the range of 0.38–0.44 nm and reveals the existence of curvature and defects (highlighted by the yellow circle). A clearly observed peak at $2\theta = 25.27^\circ$ for the CHTs is smaller than that of graphite ($2\theta = 26.54^\circ$), indicating the larger spacing interlayer of our prepared materials according to the Bragg equation (Figure S2B).²⁵ The X-ray photoelectron spectroscopy (XPS) spectrum of N 1s in Figure 4F is consistent with pyridinic (398.2 eV) and pyrrolic (400.6 eV) nitrogen.⁴⁴ The doping level of nitrogen in the CHTs is $\sim 6\%$, and the corresponding N-binding configuration contains 58.2% pyridinic N and 41.8% pyrrolic N. The electron energy loss spectroscopy (EELS) spectrum of the N-doped porous CHTs (Figure 4G) shows a carbon K-edge with a broad peak between 290 and 305 eV and a nitrogen K-edge at around 400 eV.^{45,46} The carbon K-edge exhibits a pre-peak at 285.5 eV, corresponding to the transitions from the 1s core level to π^* states in the conduction

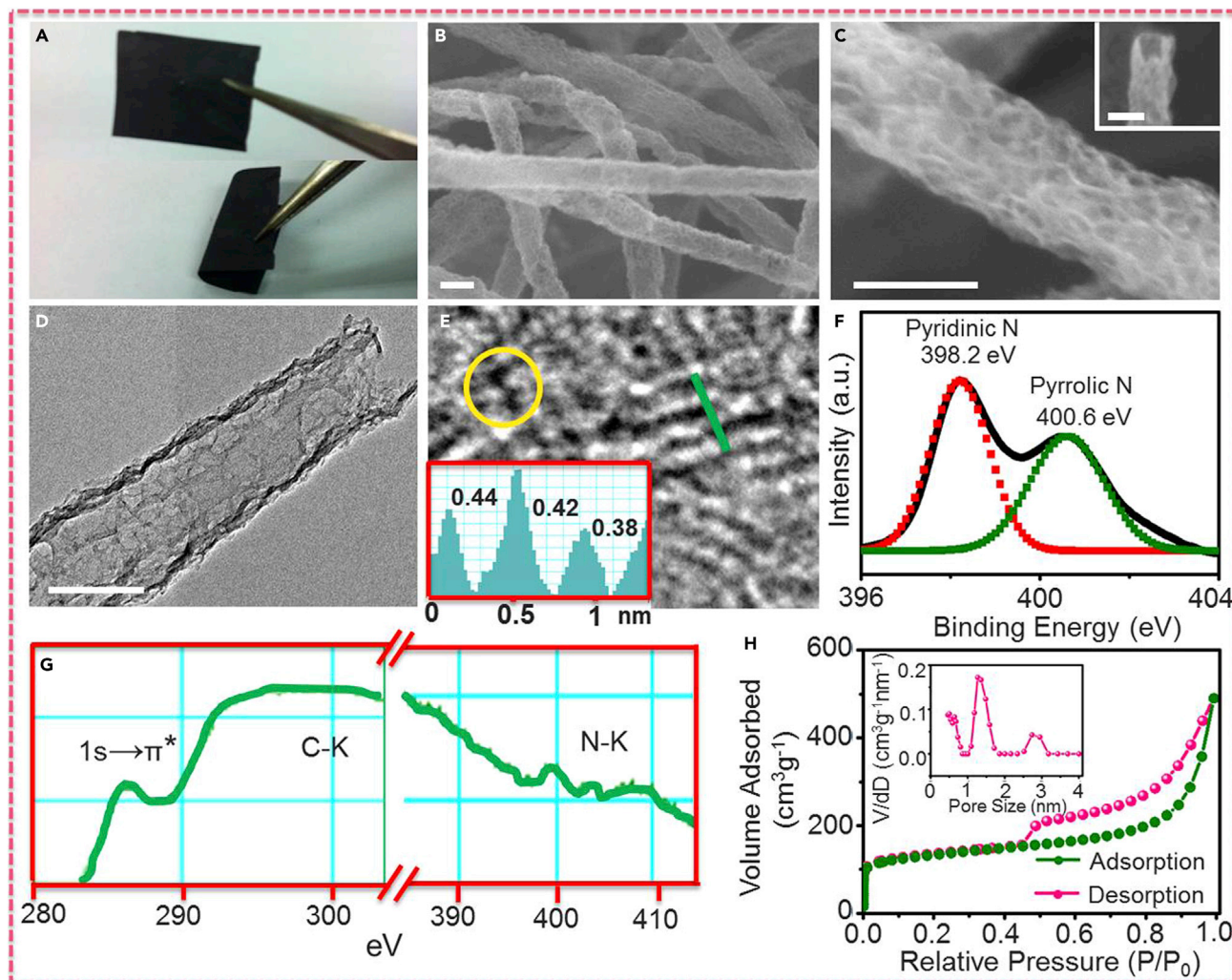


Figure 4. Characterizations of the Porous N-Doped CHTs

(A–E) Digital photograph (A), FESEM images (B and C), TEM image (D), and HRTEM image and line profile (E) of the d spacing of graphene sheets of the wall of CHTs. Scale bars: 100 nm.

(F–H) XPS spectra (F), EELS spectra (G), and nitrogen adsorption-desorption isotherms and pore-size distributions (H). In (F), black trace is data, and red and green traces correspond to fitted peaks.

See also Figures S7–S9.

band, indicating the existence of sp^2 bonding in the prepared materials.⁴⁶ Raman-spectrum analyses show that the ratio ($R \equiv I_G/I_D$) of the prepared samples is much higher than that of their counterpart from the carbonization of pure ZIF-8, but is lower than that of graphite, confirming the much enhanced graphitization of the resulting carbonaceous materials after adding $\text{Co}(\text{Ac})_2$ in the precursors, but some defects still remain in the prepared samples (Figure S8).^{22,24} We also conducted a nitrogen adsorption/desorption isotherm experiment for the N-doped porous CHTs. The specific Brunauer-Emmett-Teller surface area of the N-doped porous CHTs is $438 \text{ m}^2 \text{ g}^{-1}$, much larger than that of the CNFs ($35 \text{ m}^2 \text{ g}^{-1}$; Figure S9). The strong N_2 adsorption below the relative pressure of 0.1 implies the existence of micropores. The following increase of the sorption isotherms ranging from 0.1 to 1 is characteristic of mesopore (0.1–0.6) and macropore (0.6–1) filling in the CHTs (Figures 4H).⁴⁷ Pore-size distribution in the inset of Figure 4H shows N-doped porous CHTs with micropores peaking at ~ 0.6 and 1.5 nm , and mesopores peaking

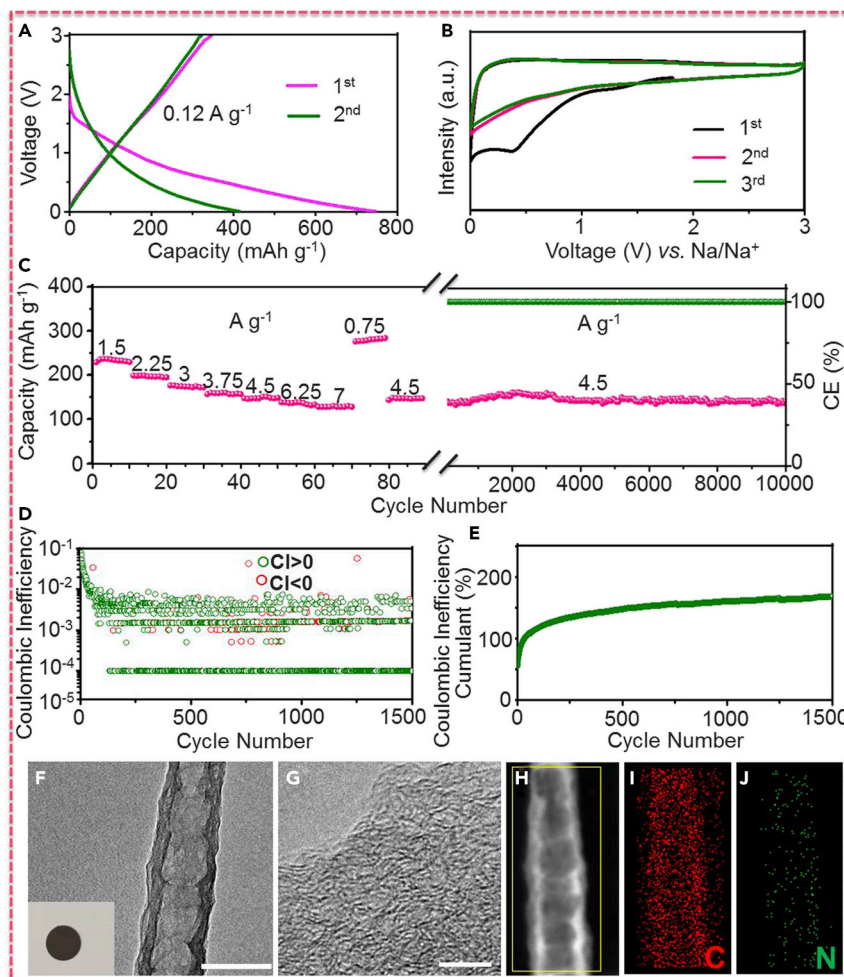


Figure 5. Electrochemical Performance of the Porous N-Doped CHTs

(A–E) Charge-discharge voltage profiles at 0.12 A g^{-1} (A), CV curves (B), rate capability and cycling performance (C), coulombic inefficiency (D), and coulombic inefficiency cumulant (E).^{52,53} (F–J) TEM image and digital photograph (inset) (F) and HRTEM image (G). A dark-field TEM image (H) and the corresponding EDX mapping (I for elemental carbon and J for elemental nitrogen) of the porous N-doped CHTs after 10,000 cycles are also shown. Scale bars: 200 nm (F) and 5 nm (G). See also Figures S10–S13.

at 3.5 nm. These results are in agreement with the TEM and HRTEM observations of a multi-level or hierarchical porous structure.⁴⁸

To examine the electrochemical performance of the N-doped CHTs, we set up coin cells with Na metal as counter electrode. Figure 5A shows the representative galvanostatic charge-discharge profiles of the as-synthesized porous CHTs in the voltage range of 0–3 V versus Na/Na^+ at the rate of 0.12 A g^{-1} . The first discharge and charge capacities were 346 and 735 mAh g^{-1} , respectively, which are much higher than that of the CNFs (Figure S10). The irreversible capacity loss of 389 mAh g^{-1} in the first cycle is mainly caused by the formation of the solid electrolyte interface (SEI) film and the decomposition reaction of the electrolyte.^{35,48,49} The volumetric capacity of the prepared samples is about 0.2 Ah cm^{-3} . Most of the capacity of the as-synthesized CHTs can be attributed to Na insertion between graphene layers with enlarged spacing and binding of Na at pores and defects.^{6,21,27,50} Moreover,

N doping is also able to enhance the electrochemical performance of the whole electrode.^{28,29,51} In the cyclic voltammogram (CV) plots (Figure 5B), one peak can be clearly identified in the first cycle, which can be assigned to the formation of SEI. The CV profiles in the following cycles overlap well, suggesting excellent reversible Na-ion storage in N-doped porous CHTs.

The N-doped porous CHTs exhibit excellent rate capability and cycle performance as shown in Figure 5C. At current densities of 1.5, 2.25, 3, 3.75, 4.5, 6.25, and 7 A g⁻¹, the reversible specific capacities of the prepared CHTs are around 238, 200, 175, 157, 147, 138, and 128 mAh g⁻¹, respectively. When the rate is reduced to 0.75 A g⁻¹, a high capacity of 284 mAh g⁻¹ can be obtained. More importantly, the electrode can manifest an outstanding cycling life over 10,000 cycles (~140 mAh g⁻¹ at 4.5 A g⁻¹) without any clear decline in capacity. In addition, this material also shows good rate capability and long-term stability between 0 and 1 V versus Na⁺/Na (Figure S11). The increase in mass loading of the prepared CHT paper slightly decreases its electrochemical performance (Figure S12).

To further address the SEI stability of the anode, we also carefully plotted the coulombic inefficiency (CI), defined as $CI \equiv 1 - CE$, and coulombic inefficiency cumulant (CIC), which is the cumulative sum of capacity-weighted individual-cycle CIs.^{52,53} The |CI| is plotted with the vertical axis in logarithmic scale (Figure 5D). Green and red circles stand for $CI > 0$ and $CI < 0$, respectively. In ~24 cycles, the CI drops to a level close to 0.01 ($CE = 99\%$). The CI can reach to 0.0001 ($CE = 99.99\%$) after 120 cycles. The best CE reported is 0.9999 or 1.0001 because of the readout precision of four decimal digits in the electrochemical testing station. It is clear that the CI can be mainly maintained in the range of 0.0015–0.0001 after 200 cycles, corresponding to 99.85%–99.99% CE. The fast decreasing trend of CI_n shows the efficient self-healing of the prepared CHTs toward nearly perfect hermiticity to avoid direct liquid electrolyte contact with any electronically conductive surface.⁵²

Figure 5E shows the CIC curve of the coin cell. The CICs increase quickly to around 100% in the first dozens of cycles. However, a very slow increase of CICs can be observed in the following cycles, indicating that a stable, hermetic SEI seal coat has formed, which serves as an in situ solid electrolyte. This shows that we should eventually be able to use a pre-sodiation procedure to pre-treat the anode and form a proper SEI solid electrolyte in the formation stage, and then expect good performance inside a Na-matched full cell later. Also, it has been recently shown that when an amorphous carbon anode is made into a Na-matched full cell, the actual full-cell capacity decay can be much more optimistic than the CIC analysis indicates (by a factor as large as 5), because of the presence of soluble redox-active species in the liquid electrolyte other than Li⁺ (J.L., unpublished data).

As shown in the digital photograph (inset of Figure 5F), it is clear that the morphology and structural integrity of the tested electrode after 10,000 cycles are well maintained without clear damage. The TEM image of the CHT electrode after cycling reveals that hollow tubular structure of the prepared carbons is still preserved. In addition, the HRTEM study shows a similar graphitic structure as the non-cycled counterparts (Figure 5G). From the EDX mapping, the N and C elements can still be found to be distributed uniformly throughout the sample (Figures 5H–5J). The results above indicate that the N-doped CHT paper maintains good mechanical integrity in cycling. Electrochemical impedance spectroscopy analysis (Figure S13) reveals that the prepared CHTs show lower charge-transfer resistance for Na⁺-ion insertion and extraction than that of CNFs.²

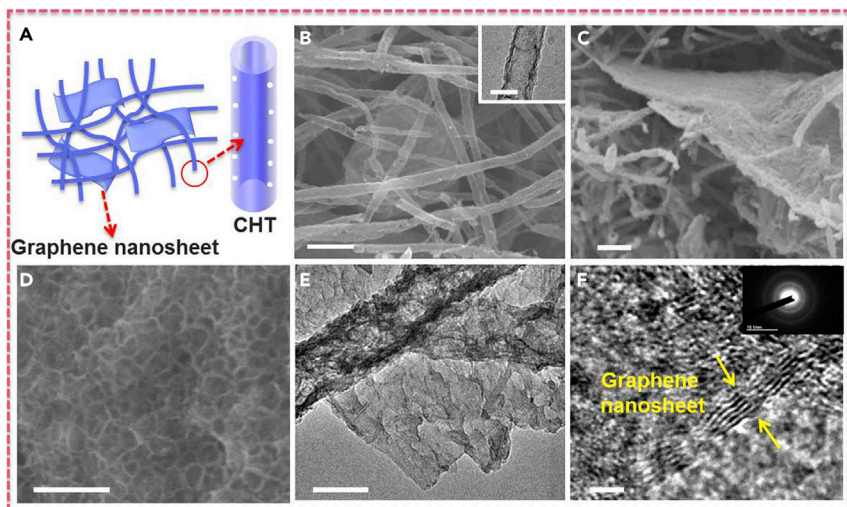


Figure 6. Characterizations of the Porous N-Doped CHT/Graphene Composites

(A) Schematic of the design.

(B–F) FESEM (B–D), TEM (E), and HRTEM (F) images of the synthesized hybrids. Scale bars: 500 nm (B and C), 100 nm (B inset, D, and E), and 2 nm (F).

See also Figures S14–S17.

DISCUSSION

Our strategy for synthesizing N-doped carbons (CNFs and CHTs) presented in this work is scalable, facile, and reproducible. Electrospinning is a common technique for introducing different metal salts into polymer nanofibers, which can serve as metal ion resources for the *in situ* growth of a layer of zeolitic imidazolate framework on composite nanofibers, yielding a core-shell nanocomposite. The core and shell play different roles in altering the composition and structure of the resulting materials. A bimetallic MOF shell was constructed by fixing two different metal salts into polymer nanofibers. The combined BMZIF can inherit all the merits of each ZIF material, which are high N-doping content and porous structure from ZIF-8 and well-graphitized carbon from ZIF-67. The metal salt in the composite can be used not only for the formation of ZIFs but also to provide the source (metal oxide) for etching the carbon core (carbonized from the PAN polymer) into a hollow tubular structure. As a result, a series of 1D nanocarbons (spanning from CNFs to CHTs) with N doping, porous structure, and high graphitization can be obtained. More importantly, such a simple approach can also be extended to the synthesis of other porous N-doped CHT-based composites; for example, porous N-doped CHT/graphene formed by sandwiching porous graphene nanosheets between CHTs (Figure 6 and Figures S14–S17).

The porous N-doped CHTs show remarkable electrochemical performance as an anode for SIBs, as a result of the unique nanostructure and N doping that facilitate Na⁺-ion transport. To the best of our knowledge, the performance is much better than that of other carbonaceous anodes (Table S1). The performance of our porous N-doped CHTs results from the following features: (1) the carbon layers with enlarged *d* spacing and numerous defects and pores that act as reservoirs for storing the Na ions,^{6,25,54,55} (2) a high surface area and porous structure, providing a short diffusion distance for Na ions and sufficient contact between active material and electrolyte for a rapid charge-transfer reaction,¹¹ and (3) long-aspect-ratio tubular structures that facilitate fast 1D electron transport and electrical percolation.^{9,28,55,56}

Moreover, many defects in the CHTs also assist the diffusion of Na^+ from outer carbon to inner carbon for quick activation of all the carbon host materials.²⁴

In summary, we report a simple and original approach to the synthesis of a series of nanocarbons (CNFs and CHTs) with N doping, porous structure, and high graphitization. This approach relies on the growth of a bimetallic MOF on the PAN nanofibers containing metal acetates. The various factors that control the electrochemical performance of the carbonaceous material, such as a multi-level hierarchical porous structure, degree of graphitization, large enough interlayer spacing, and N doping, can all be systematically adjusted. Benefiting from the combined improvements, the N-doped porous CHTs exhibit exceptional electrochemical performance as an anode material for SIBs with high capacity up to 346 mAh g^{-1} , good rate capability, and ultralong cycle life up to 10,000 cycles without clear decline in capacity.

EXPERIMENTAL PROCEDURES

Synthesis of the Bimetallic Zeolitic Imidazolate Framework Shell onto PAN/ $\text{Zn}(\text{Ac})_2/\text{Co}(\text{Ac})_2$ Composite Nanofibers

The electrospinning solution was synthesized by dissolving 1 g of PAN (Aldrich) and a specific amount of metal acetate (1.89 g of $\text{Zn}(\text{Ac})_2 \cdot 2\text{H}_2\text{O}$ and 0.107 g of $\text{Co}(\text{Ac})_2 \cdot 4\text{H}_2\text{O}$) in 30 mL of DMF (Aldrich) solvent. The working voltage, electrospinning distance, and flow rate were fixed at 17 kV, 0.05 mm min⁻¹, and 20 cm, respectively. The prepared PAN/ $\text{Zn}(\text{Ac})_2/\text{Co}(\text{Ac})_2$ composite films were added into ethanol solution containing 2-methylimidazole (0.65 g, Aldrich) and then maintained at room temperature for 12 hr to grow a layer of BMZIF onto the composite nanofibers.

Synthesis of N-Doped Porous CHTs with High Graphitization

The composite films obtained were heated in inert gas at 700°C for 20 hr at a heating rate of 2°C min⁻¹, followed by a simple acid treatment to remove the residual metal, leading to the formation of N-doped porous CHTs containing ~3.7 wt % oxygen, 6.0 wt % nitrogen, and 90.3 wt % carbon. In addition, the structure of the resulting materials can be changed from porous CNFs to CHTs by controlling the content of $\text{Zn}(\text{Ac})_2$ in the precursor.

In Situ TEM

In situ TEM experiments in this work were carried out on a double-tilted platform (Protobricks Aduro) with a heating E-chip specimen support that enables high resolution at high temperature. The prepared sample was loaded onto a carbon membrane supported by a Si E-Chip, followed by a heating treatment up to 700°C at a rate of 10°C min⁻¹. TEM studies were carried out on a JEM-2010F transmission electron microscope at 200 kV.

Other Characterizations

The as-prepared materials were characterized by TEM, HRTEM, EELS spectrometry (Gatan, Enfina), FESEM (JEOL-6700), XRD (Rigaku), XPS (PHI5600), EDX spectroscopy (Oxford), and nitrogen sorption measurement at 77 K (ASAP 2020).

Electrochemical Measurements

The battery tests were evaluated in two-electrode 2032 coin cells. The prepared porous N-doped CHT paper was easily punched and then directly loaded as the working electrode without binder and carbon black. The weight of the prepared CHT paper was around 0.36 mg cm^{-2} . Sodium foil, glass fiber film (Whatman), and 1 M NaPF_6 in a 50:50 (w/w) mixture of ethylene carbonate and diethyl carbonate were used as the SIB counter/reference electrode, the separator, and the electrolyte,

respectively. The charging-discharging tests were carried out with a LAND battery tester. CV and electrochemical impedance measurements were performed on a CHI 660D electrochemical workstation.

SUPPLEMENTAL INFORMATION

Supplemental Information includes 17 figures and 1 table and can be found with this article online at <http://dx.doi.org/10.1016/j.chempr.2017.05.021>.

AUTHOR CONTRIBUTIONS

Y.M.C., X.Y.L., H.T.H., J.L., and J.B.G. conceived the idea and co-wrote the manuscript. Y.M.C. and X.Y.L. carried out the synthesis, material characterizations, and electrochemical evaluation. Y.M.C. and W.L. conducted *in situ* TEM testing. K.P., C.W., W.J.X., F.Y., J.Z., L.M.S., and T.Q.L. helped with the material characterizations.

ACKNOWLEDGMENTS

H.H. acknowledges financial support from the Hong Kong Polytechnic University (project nos. 1-ZVGH and 1-YW1A). J.L. acknowledges support from National Science Foundation grant ECCS-1610806. J.B.G. thanks the Robert A. Welch Foundation (grant F-1066).

Received: March 16, 2017

Revised: April 22, 2017

Accepted: May 26, 2017

Published: July 13, 2017

REFERENCES AND NOTES

- Armand, M., and Tarascon, J.M. (2008). Building better batteries. *Nature* **451**, 652–657.
- Chen, Y.M., Yu, X.Y., Li, Z., Paik, U., and Lou, X.W. (2016). Hierarchical MoS₂ tubular structures internally wired by carbon nanotubes as a highly stable anode material for lithium-ion batteries. *Sci. Adv.* **2**, 21600021.
- Tarascon, J.M., and Armand, M. (2001). Issues and challenges facing rechargeable lithium batteries. *Nature* **414**, 359–367.
- Yao, X., and Zhao, Y. (2017). Three-dimensional porous graphene networks and hybrids for lithium-ion batteries and supercapacitors. *Chem* **2**, 171–200.
- Sun, Y., Zheng, G.Y., She, Z.W., Liu, N., Wang, S., Sun, J., Lee, H.R., and Cui, Y. (2016). Graphite-encapsulated Li-metal hybrid anodes for high-capacity Li batteries. *Chem* **1**, 287–297.
- Wen, Y., He, K., Zhu, Y., Han, F., Xu, Y., Matsuda, I., Ishii, Y., Cumings, J., and Wang, C. (2014). Expanded graphite as superior anode for sodium-ion batteries. *Nat. Commun.* **5**, 4033.
- Zhang, B., Kang, F., Tarascon, J.M., and Kim, J.K. (2016). Recent advances in electrospun carbon nanofibers and their application in electrochemical energy storage. *Prog. Mater. Sci.* **76**, 319–380.
- Choi, J.W., and Aurbach, D. (2016). Promise and reality of post-lithium-ion batteries with high energy densities. *Nat. Rev. Mater.* **1**, 16013.
- Chen, Y., Li, X., Park, K., Zhou, L., Huang, H., Mai, Y.W., and Goodenough, J.B. (2016). Hollow nanotubes of N-doped carbon on CoS. *Angew. Chem. Int. Ed.* **55**, 15831–15834.
- Luo, W., Shen, F., Bommier, C., Zhu, H., Ji, X., Hu, L., et al. (2016). Na-ion battery anodes: materials and electrochemistry. *Acc. Chem. Res.* **49**, 231–240.
- Zhang, K., Park, M., Zhou, L., Lee, G.H., Shin, J., Hu, Z., Chou, S.L., Chen, J., and Kang, Y.M. (2016). Cobalt-doped FeS₂ nanospheres with complete solid solubility as a high-performance anode material for sodium-ion batteries. *Angew. Chem. Int. Ed.* **128**, 13014–13018.
- Chao, D., Zhu, C., Yang, P., Xia, X., Liu, J., Wang, J., Fan, X., Savilov, S.V., Lin, J., Fan, H.J., et al. (2016). Array of nanosheets render ultrafast and high-capacity Na-ion storage by tunable pseudocapacitance. *Nat. Commun.* **7**, 12122.
- Cui, J., Yao, S., and Kim, J.K. (2017). Recent progress in rational design of anode materials for high-performance Na-ion batteries. *Energy Storage Mater.* **7**, 64–114.
- Li, X., Chen, Y., Huang, H., Mai, Y.W., and Zhou, L. (2016). Electrospun carbon-based nanostructured electrodes for advanced energy storage – a review. *Energy Storage Mater.* **5**, 58–92.
- Kong, B., Zu, L., Peng, C., Zhang, Y., Zhang, W., Tang, J., Selomulya, C., Zhang, L., Chen, H., Wang, Y., et al. (2016). Direct superassemblies of freestanding metal–carbon frameworks featuring reversible crystalline-phase transformation for electrochemical sodium storage. *J. Am. Chem. Soc.* **138**, 16533–16541.
- Cao, Y., Xiao, L., Sushko, M.L., Wang, W., Schwenzer, B., Xiao, J., Nie, Z., Saraf, L.V., Yang, Z., and Liu, J. (2012). Sodium ion insertion in hollow carbon nanowires for battery applications. *Nano Lett.* **12**, 3783–3787.
- Wenzel, S., Hara, T., Janek, J., and Adelhelm, P. (2011). Room-temperature sodium-ion batteries: improving the rate capability of carbon anode materials by templating strategies. *Energy Environ. Sci.* **4**, 3342–3345.
- Tang, K., Fu, L.J., White, R.J., Yu, L.H., Titirici, M.M., Antonietti, M., and Maier, J. (2012). Hollow carbon nanospheres with superior rate capability for sodium-based batteries. *Adv. Energy Mater.* **2**, 873–877.
- Wu, L., Buchholz, D., Vaalma, C., Giffin, G.A., and Passerini, S. (2016). Apple-biowaste-derived hard carbon as a powerful anode material for Na-ion batteries. *ChemElectroChem* **3**, 292–298.

20. Cao, B., Liu, H., Xu, B., Lei, Y.F., Chen, X.H., and Song, H.H. (2016). Mesoporous soft carbon as an anode material for sodium ion batteries with superior rate and cycling performance. *J. Mater. Chem. A* 4, 6472–6478.
21. Zhang, B., Ghimbeu, C.M., Laberty, C., Vix-Guterl, C., and Tarascon, J.M. (2016). Correlation between microstructure and Na storage behavior in hard carbon. *Adv. Energy Mater.* 6, 1501588.
22. Chen, Y., Lu, Z., Zhou, L., Mai, Y.W., and Huang, H. (2012). Triple-coaxial electrospun amorphous carbon nanotubes with hollow graphitic carbon nanospheres for high-performance Li ion batteries. *Energy Environ. Sci.* 5, 7898–7902.
23. Chen, Y., Li, X., Park, K., Song, J., Hong, J., Zhou, L., Mai, Y.W., Huang, H., and Goodenough, J.B. (2013). Hollow carbon-nanotube/carbon-nanofiber hybrid anodes for Li-ion batteries. *J. Am. Chem. Soc.* 135, 16280–16283.
24. Chen, Y., Li, X., Zhou, X., Yao, H., Huang, H., Mai, Y.W., and Zhou, L. (2014). Hollow-tunneled graphitic carbon nanofibers through Ni-diffusion-induced graphitization as high-performance anode materials. *Energy Environ. Sci.* 7, 2689–2696.
25. Yu, Z.L., Xin, S., You, Y., Yu, L., Lin, Y., Xu, D.W., Qiao, C., Huang, Z.H., Yang, N., Yu, S.H., et al. (2016). Ion-catalyzed synthesis of microporous hard carbon embedded with expanded nanographite for enhanced lithium/sodium storage. *J. Am. Chem. Soc.* 138, 14915–14922.
26. Wu, R., Wang, D.P., Rui, X., Liu, B., Zhou, K., Law, A.W., Yan, Q., Wei, J., and Chen, Z. (2015). In-situ formation of hollow hybrids composed of cobalt sulfides embedded within porous carbon polyhedra/carbon nanotubes for high-performance lithium-ion batteries. *Adv. Mater.* 27, 3038–3044.
27. Paraknowitsch, J.P., and Thomas, A. (2013). Doping carbons beyond nitrogen: an overview of advanced heteroatom doped carbons with boron, sulphur and phosphorus for energy applications. *Energy Environ. Sci.* 6, 2839–2855.
28. Wang, Z., Qie, L., Yuan, L., Zhang, W., Hu, X., and Huang, Y. (2013). Functionalized N-doped interconnected carbon nanofibers as an anode material for sodium-ion storage with excellent performance. *Carbon* 55, 328–334.
29. Song, H., Li, N., Cui, H., and Wang, C. (2014). Enhanced storage capability and kinetic processes by pores- and hetero-atoms- riched carbon nanobubbles for lithium-ion and sodium-ion batteries anodes. *Nano Energy* 4, 81–87.
30. Jeong, H.M., Lee, J.W., Shin, W.H., Choi, Y.J., Shin, H.J., Kang, J.K., and Choi, J.W. (2011). Nitrogen-doped graphene for high-performance ultracapacitors and the importance of nitrogen-doped sites at basal planes. *Nano Lett.* 11, 2472–2477.
31. Shin, W.H., Jeong, H.M., Kim, B.G., Kang, J.K., and Choi, J.W. (2012). Nitrogen-doped multiwall carbon nanotubes for lithium storage with extremely high capacity. *Nano Lett.* 12, 2283–2288.
32. Chen, Y.Z., Wang, C., Wu, Z.Y., Xiong, Y., Xu, Q., Yu, S.H., and Jiang, H.L. (2015). From bimetallic metal-organic framework to porous carbon: high surface area and multicomponent active dopants for excellent electrocatalysis. *Adv. Mater.* 27, 5010–5016.
33. Stassen, I., Styles, M., Greci, G., Gorp, H.V., Vanderlinde, W., Feyter, S.D., Falcaro, P., Vos, D.D., Vereeken, P., and Ameloot, R. (2016). Chemical vapour deposition of zeolitic imidazolate framework thin films. *Nat. Mater.* 15, 304–310.
34. Zhang, W., Wu, Z.Y., Jiang, H.L., and Yu, S.H. (2014). Nanowire-directed templating synthesis of metal-organic framework nanofibers and their derived porous doped carbon nanofibers for enhanced electrocatalysis. *J. Am. Chem. Soc.* 136, 14385–14388.
35. Xu, J., Wang, M., Wickramaratne, N.P., Jaroniec, M., Dou, S., and Dai, L. (2015). High-performance sodium ion batteries based on a 3D anode from nitrogen-doped graphene foams. *Adv. Mater.* 27, 2042–2048.
36. Jin, J.E., Lee, J.H., Choi, J.H., Jang, H.K., Na, J., Whang, D., Kim, D.H., and Kim, G.T. (2016). Catalytic etching of monolayer graphene at low temperature via carbon oxidation. *Phys. Chem. Chem. Phys.* 18, 101–109.
37. Kim, C., Ngoc, B.T.N., Yang, K.S., Kojima, M., Kim, Y.A., Kim, Y.J., Endo, M., and Yang, S.C. (2007). Self-sustained thin webs consisting of porous carbon nanofibers for supercapacitors via the electrospinning of polyacrylonitrile solutions containing zinc chloride. *Adv. Mater.* 19, 2341–2346.
38. Wang, H., Zhu, Q.L., Zou, R., and Xu, Q. (2017). Metal-organic frameworks for energy applications. *Chem* 2, 52–80.
39. Li, B., and Chen, B. (2016). Fine-tuning porous metal-organic frameworks for gas separations at will. *Chem* 1, 669–671.
40. Li, B., Wen, H.M., Zhou, W., Xu, Jeff Q., and Chen, B. (2016). Porous metal-organic frameworks: promising materials for methane storage. *Chem* 1, 557–580.
41. Wang, G., Li, Z., Li, M., Chen, C., Lv, S., and Liao, J. (2016). Aqueous phase synthesis and enhanced field emission properties of ZnO-sulfide heterojunction nanowires. *Sci. Rep.* 6, 29470.
42. Chen, Y., Lu, Z., Zhou, L., Mai, Y.W., and Huang, H. (2012). In situ formation of hollow graphitic carbon nanospheres in electrospun amorphous carbon nanofibers for high-performance Li-based batteries. *Nanoscale* 4, 6800–6805.
43. Wu, H., Chan, G., Choi, J.W., Ryu, I., Yao, Y., McDowell, M.T., Lee, S.W., Jackson, A., Yang, Y., Hu, L., et al. (2012). Stable cycling of double-walled silicon nanotube battery anodes through solid-electrolyte interphase control. *Nat. Nanotechnol.* 7, 310–315.
44. Wu, Z.S., Ren, W., Xu, L., Li, F., and Cheng, H.M. (2011). Doped graphene sheets as anode materials with superhigh rate and large capacity for lithium ion batteries. *ACS Nano* 5, 5463–5471.
45. He, M., Zhou, S., Zhang, J., Liu, Z., and Robinson, C. (2005). CVD growth of N-doped carbon nanotubes on silicon substrates and its mechanism. *J. Phys. Chem. B* 109, 9275–9279.
46. Schlittler, R.R., Seo, J.W., Gimzewski, J.K., Durkan, C., Saifullah, M.S., and Welland, M.E. (2001). Single crystals of single-walled carbon nanotubes formed by self-assembly. *Science* 292, 1136–1139.
47. Zhang, L.L., Zhao, X., Stoller, M.D., Zhu, Y., Ji, H., Murali, S., Wu, Y., Perales, S., Clevenger, B., and Ruoff, R.S. (2012). Highly conductive and porous activated reduced graphene oxide films for high-power supercapacitors. *Nano Lett.* 12, 1806–1812.
48. Zhang, F., Yao, Y., Wan, J., Henderson, D., Zhang, X., and Hu, L. (2017). High temperature carbonized grass as a high performance sodium ion battery anode. *ACS Appl. Mater. Interfaces* 9, 391–397.
49. Licht, S., Douglas, A., Ren, J., Carter, R., Lefler, M., and Pint, C.L. (2016). Carbon nanotubes produced from ambient carbon dioxide for environmentally sustainable lithium-ion and sodium-ion battery anodes. *ACS Cent. Sci.* 2, 162–168.
50. Wang, S., Xia, L., Yu, L., Zhang, L., Wang, H., and Lou, X.W. (2016). Free-standing nitrogen-doped carbon nanofiber films: integrated electrodes for sodium-ion batteries with ultralong cycle life and superior rate capability. *Adv. Energy Mater.* 6, 1502217.
51. Liu, H., Jia, M., Sun, N., Cao, B., Chen, R., Zhu, Q., Wu, F., Qiao, N., and Xu, B. (2015). Nitrogen-rich mesoporous carbon as anode material for high-performance sodium-ion batteries. *ACS Appl. Mater. Interfaces* 7, 27124–27130.
52. Jin, Y., Li, S., Kushima, A., Zheng, X., Sun, Y., Xie, J., Sun, J., Xue, W., Zhou, G., Wu, J., et al. (2017). Self-healing SEI enables full-cell cycling of a silicon-majority anode with a coulombic efficiency exceeding 99.9%. *Energy Environ. Sci.* 10, 580–592.
53. Wang, S., Yang, Y., Quan, W., Hong, Y., Zhang, Z., Tang, Z., and Li, J. (2017). Ti³⁺-free three-phase Li₄Ti₅O₁₂/TiO₂ for high-rate lithium ion batteries: capacity and conductivity enhancement by phase boundaries. *Nano Energy* 32, 294–301.
54. Cohn, A.P., Share, K., Carter, R., Oakes, L., and Pint, C.L. (2016). Ultrafast solvent-assisted sodium ion intercalation into highly crystalline few-layered graphene. *Nano Lett.* 16, 543–548.
55. Chen, Y., Dong, J., Qiu, L., Li, X., Li, Q., Wang, H., Liang, S., Yao, H., Huang, H., Gao, H., et al. (2017). A catalytic etching-wetting-dewetting mechanism in the formation of hollow graphitic carbon fiber. *Chem* 2, 299–310.
56. Chen, Y.M., Yu, L., and Lou, X.W. (2016). Hierarchical tubular structures composed of Co₃O₄ hollow nanoparticles and carbon nanotubes for lithium storage. *Angew. Chem. Int. Ed.* 55, 5990–5993.

Supplemental Information

Nitrogen-Doped Carbon for Sodium-Ion Battery

**Anode by Self-Etching and Graphitization
of Bimetallic MOF-Based Composite**

Yuming Chen, Xiaoyan Li, Kyusung Park, Wei Lu, Chao Wang, Weijiang Xue, Fei Yang, Jiang Zhou, Liumin Suo, Tianquan Lin, Haitao Huang, Ju Li, and John B. Goodenough

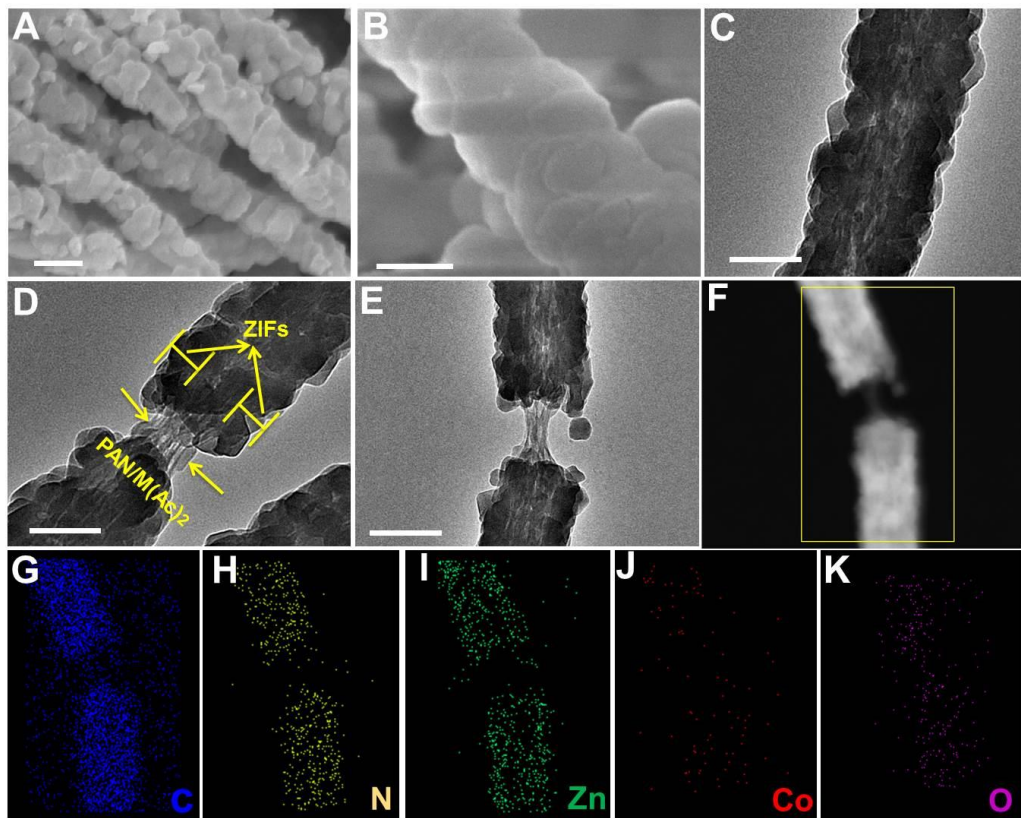


Figure S1. TEM characterization of the core-shell PAN/M(Ac)₂@BMZIF composite nanofibers, Related to Figure 1. FESEM (A, B), TEM (C-E) and EDX mapping (F-K) of the core-shell PAN/M(Ac)₂@BMZIF composite nanofibers. Scale bars, (A, E) 200 nm and (B-D) 100 nm.

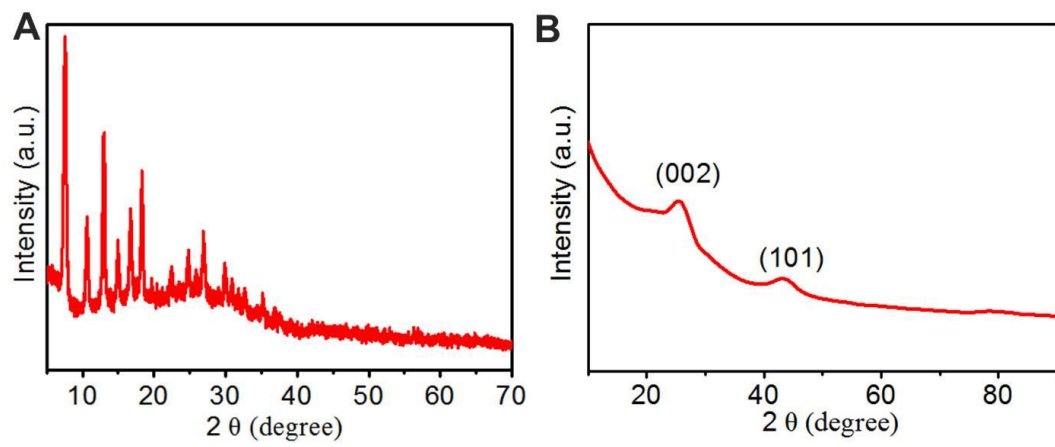


Figure S2. XRD patterns of (A) the core-shell PAN/M(Ac)₂@BMZIF composite nanofibers and (B) the CHTs, Related to Figure 1.

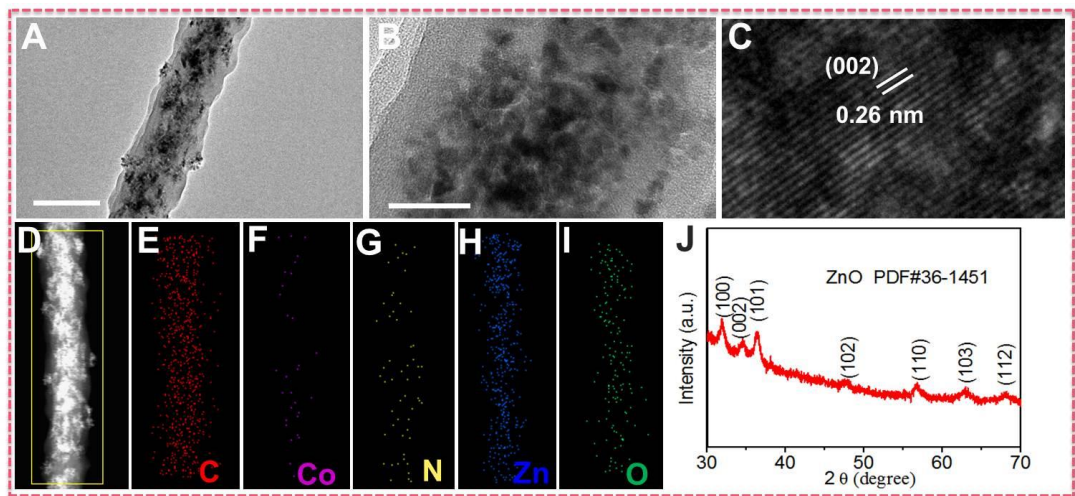


Figure S3. TEM, EDX and XRD characterization of the composite nanofibers, Related to Figure 2. (A, B) TEM and (C) HRTEM images, (D-I) EDX mapping and (J) XRD pattern of the PAN/M(Ac)₂ composite nanofibers after calcination at 500 °C in inert gas. Scale bars, (A, B) 200 nm.

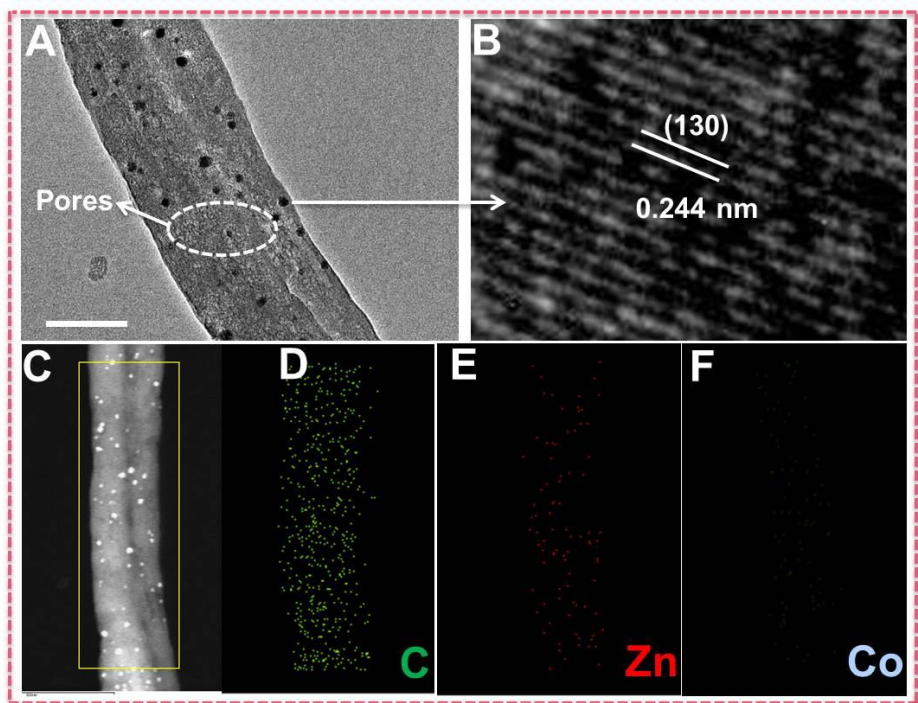


Figure S4. (A) TEM and (B) HRTEM images, (C-E) EDX mapping of the PAN/M(Ac)₂ composite nanofibers after calcination at 700 °C, Related to Figure 2. Scale bar, (A) 100 nm.

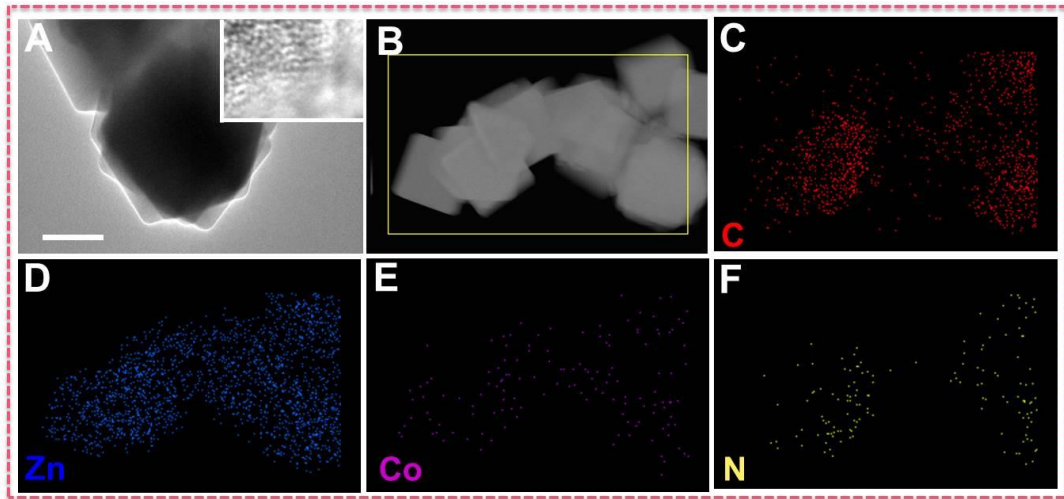


Figure S5. (A) TEM image, (B-F) EDX mapping of the ZIFs after calcination at 700 °C, Related to Figure 2. Scale bar, (A) 500 nm.

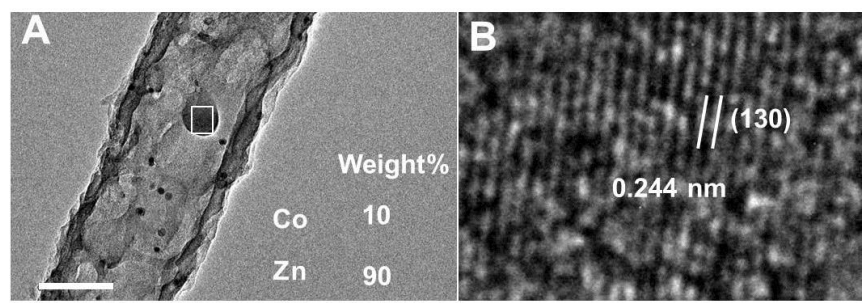


Figure S6. (A) TEM and (B) HRTEM images of the prepared CHTs without acid treatment, Related to Figure 3. Scale bar, (A) 100 nm.

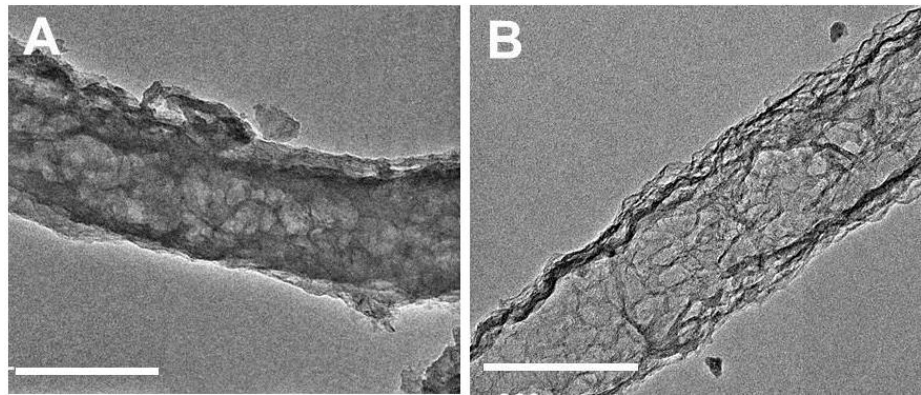


Figure S7. TEM images of the carbonaceous materials from the decomposition of BMZIFs at (A) 600 °C and (B) 800 °C, Related to Figure 4. Scale bars, (A, B) 200 nm.

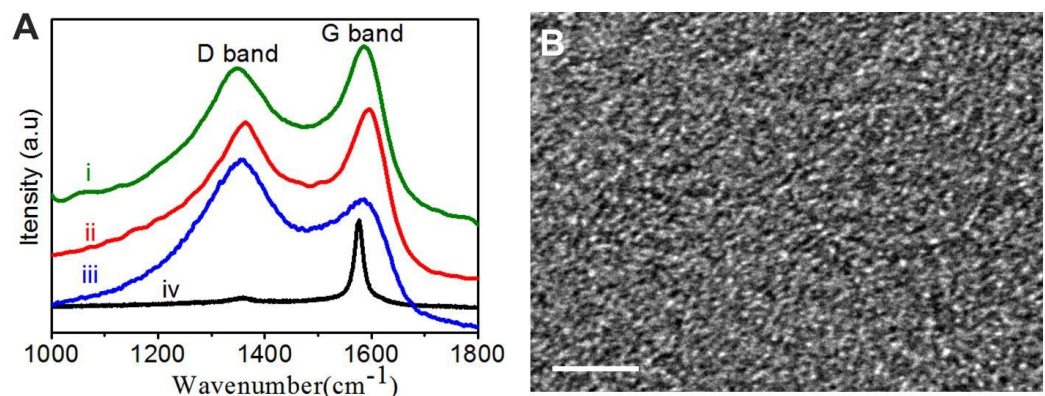


Figure S8. (A) Raman spectra of (i) CHTs and (ii) porous carbon nanofibers from the carbonization of BMZIFs, (iii) 1D carbons from the carbonization of ZIF-8, and (iv) commercial graphite. **(B)** HRTEM image of 1D carbons from the carbonization of ZIF-8, Related to Figure 4. Scale bar, **(B)** 5 nm.

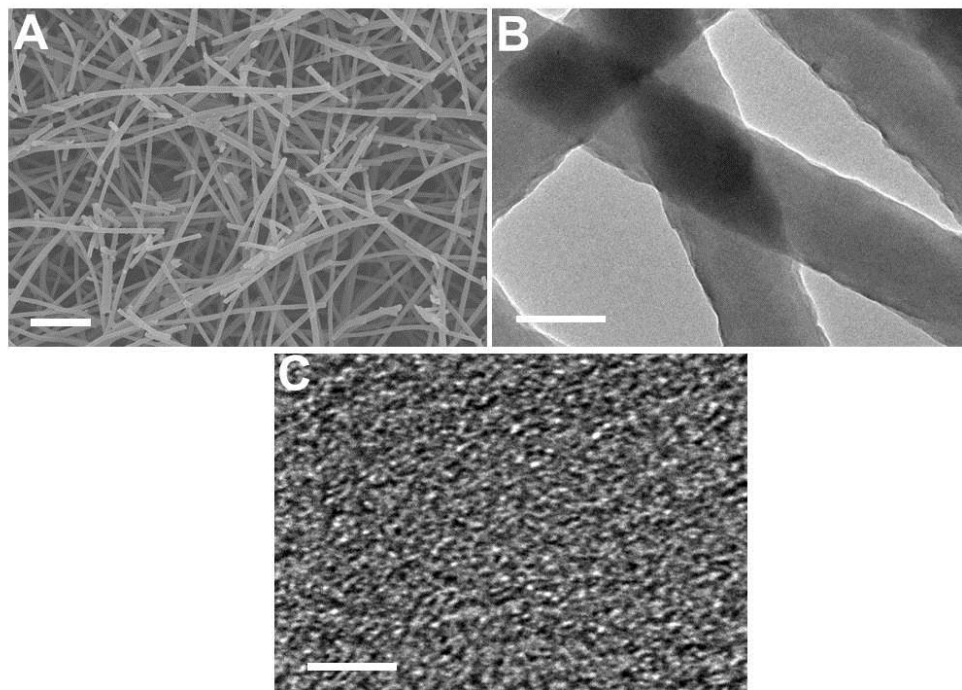


Figure S9. (A) FESEM, (B) TEM, and (C) HRTEM images of the prepared CNFs by electrospinning, Related to Figure 4. Scale bars, (A) 2 μ m, (B) 200 nm, and (C) 2 nm.

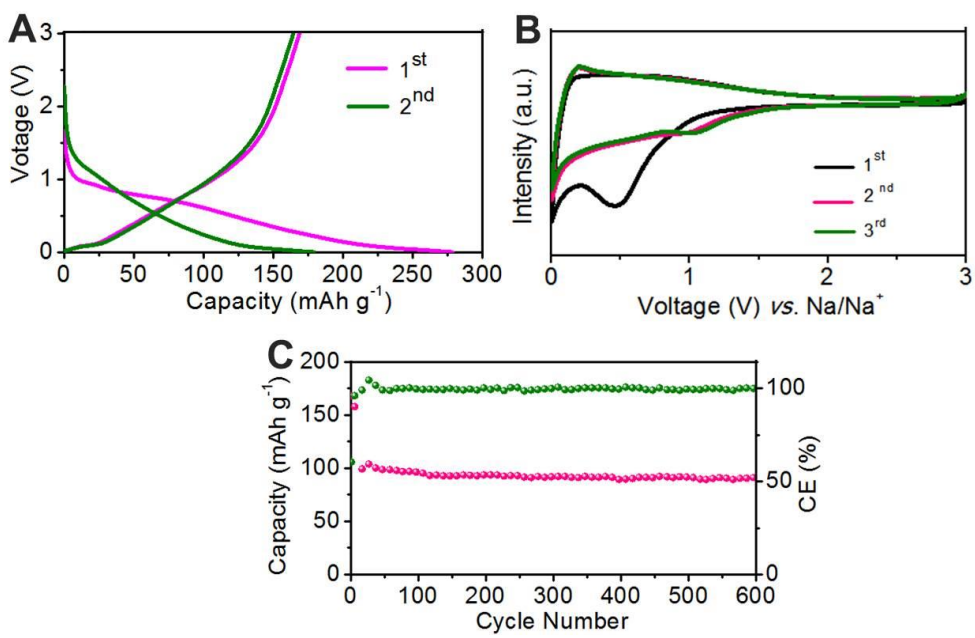


Figure S10. (A) Charge-discharge profiles at 0.12 A g^{-1} , (B) CV curves, and (C) cycling life at 1 A g^{-1} of the CNFs, Related to Figure 5.

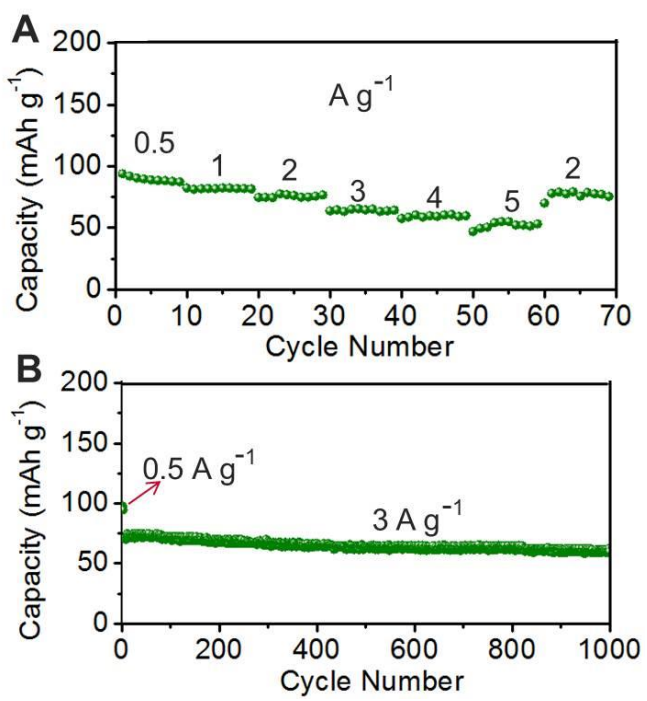


Figure S11. Electrochemical performance of the prepared CHTs in the voltage range of 0-1 V, Related to Figure 5. (A) Rate capability and (B) cycling life.

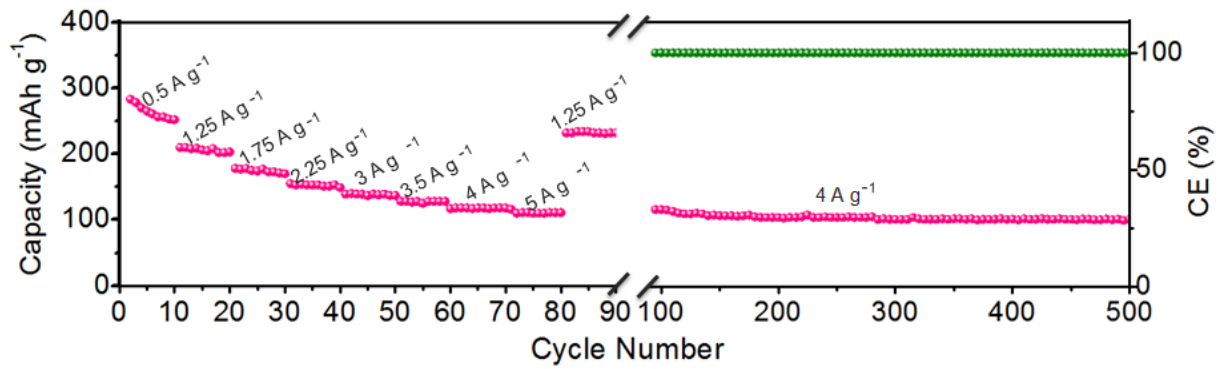


Figure S12. Electrochemical performance of the prepared CHTs with a high mass loading of $\sim 2 \text{ mg cm}^{-2}$, Related to Figure 5. Rate capability and cycling life.

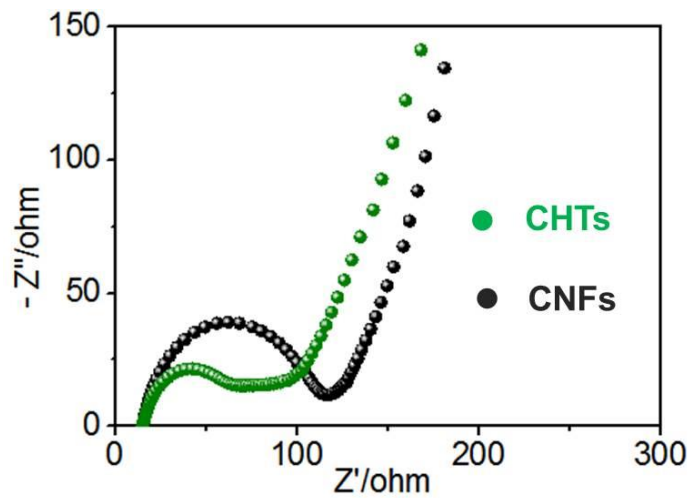


Figure S13. Nyquist plots of the prepared samples, Related to Figure 5.

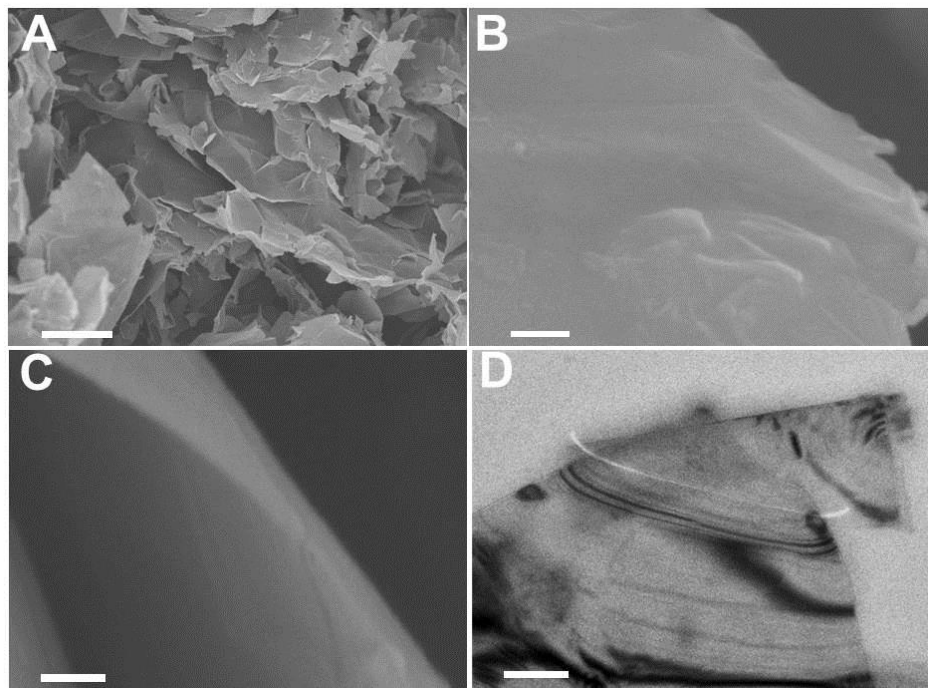


Figure S14. (A-C) FESEM and (D) TEM images of graphene nanosheets, Related to Figure 6. Scale bars, (A) 5 μ m, (B) 100 nm, (C) 50 nm, and (D) 500 nm.

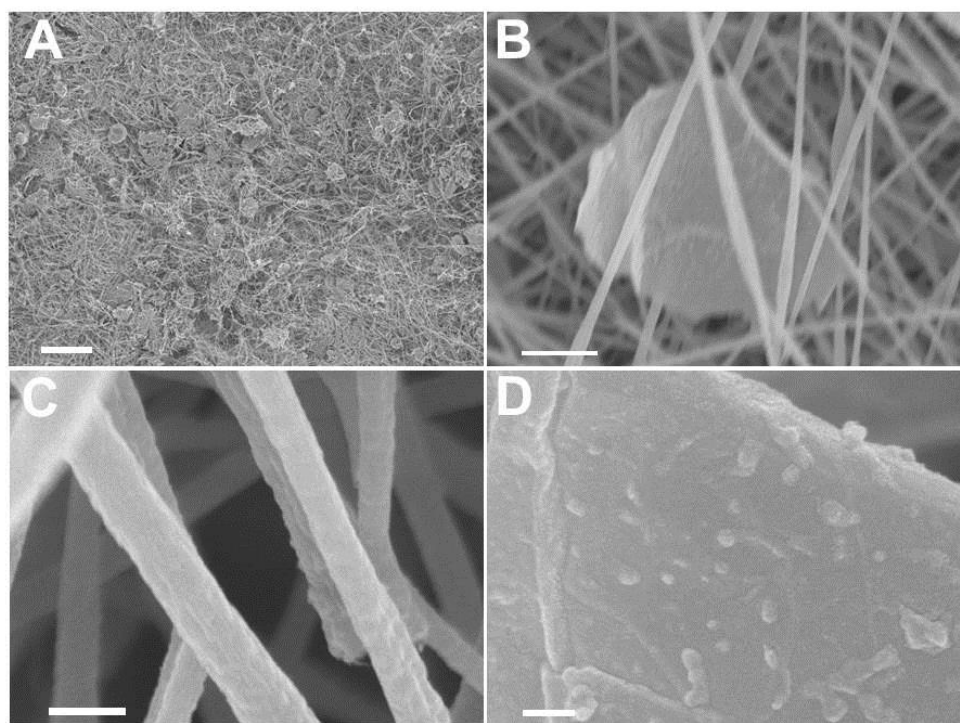


Figure S15. (A-D) FFSEM images of PAN/M(Ac)₂/graphene composite, Related to Figure 6. Scale bars, (A) 20 μm , (B) 1 μm , (C) 200 nm, and (D) 100 nm.

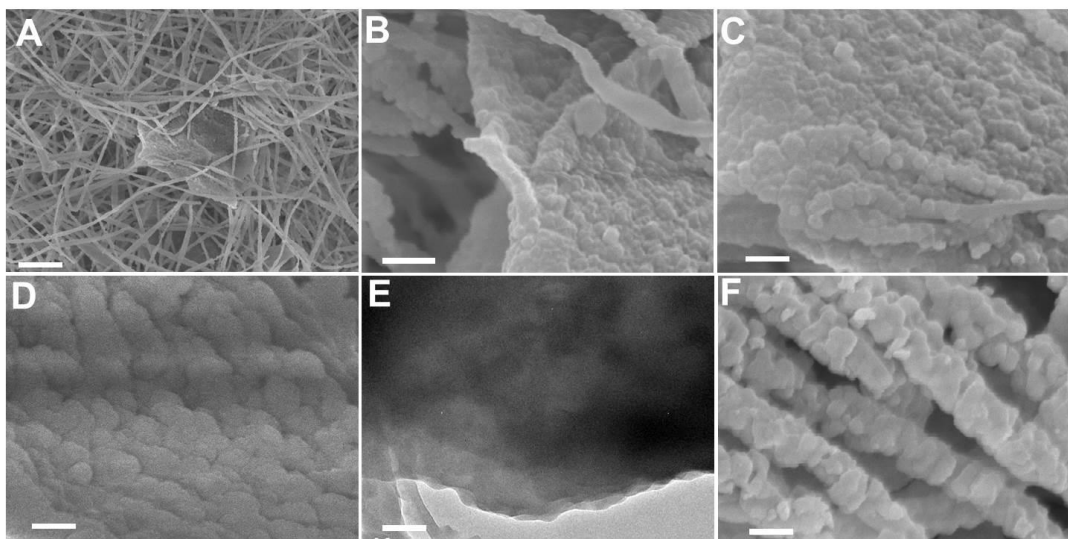


Figure S16. (A-D, F) FESEM and (E) TEM images of the as-prepared BMZIF/PAN/graphene composites, Related to Figure 6. Scale bars, (A) 2 μ m, (B) 500 nm, (C, F) 200 nm, and (D, E) 100 nm.

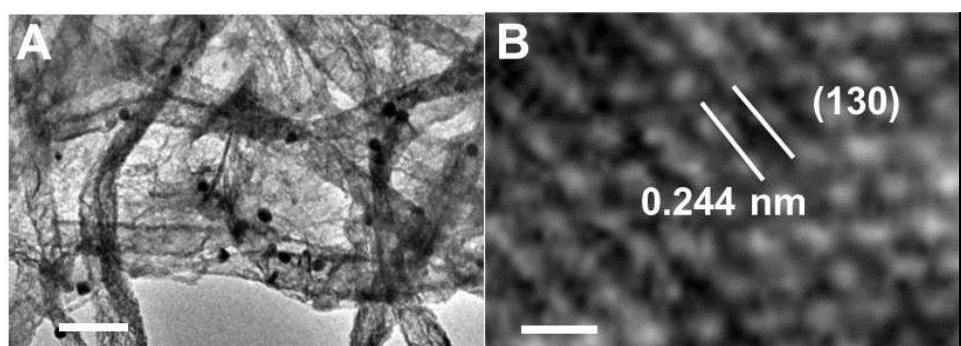


Figure S17. (A) TEM and (B) HRTEM images of the as-prepared BMZIF/PAN/graphene composites after calcination, Related to Figure 6.
Scale bars, (A, B) 500 nm.

Table S1. Electrochemical properties of different carbonaceous-based electrodes.

Reference	Type of materials	Gravimetric capacity	Volumetric capacity	Cycling number
This work	N-doped porous CHT	346 mAh g ⁻¹ at 0.12 A g ⁻¹	0.2 Ah cm ³	10000
		284 mAh g ⁻¹ at 0.75 A g ⁻¹		
		238 mAh g ⁻¹ at 1.5 A g ⁻¹		
1	Expanded graphene nanosheets	180 mAh g ⁻¹ at 0.1 A g ⁻¹	No report	2000
2	Porous CNFs	225 mAh g ⁻¹ at 0.05 A g ⁻¹	No report	50
3	CNTs	130 mAh g ⁻¹ at 0.1 A g ⁻¹	No report	600
4	N,O co-doped carbon bubbles	130 mAh g ⁻¹ at 0.1 A g ⁻¹ 80 mAh g ⁻¹ at 0.2 A g ⁻¹	No report	85
5	Hollow CNFs	280 mAh g ⁻¹ at 0.05A g ⁻¹	No report	290
6	Few-layered graphene	140 mAh g ⁻¹ at 1A g ⁻¹	No report	8000
7	Hollow CNFs	270 mAh g ⁻¹ at 0.05A g ⁻¹	No report	200
8	N-doped mesoporous carbon	338 mAh g ⁻¹ at 0.03A g ⁻¹ 110.7 mAh g ⁻¹ at 0.5A g ⁻¹	No report	800
9	POx-doped hard carbon	250 mAh g ⁻¹ at 0.1A g ⁻¹ 50 mAh g ⁻¹ at 1A g ⁻¹	No report	150
10	Hard carbon	200 mAh g ⁻¹ at 0.2A g ⁻¹	No report	300
11	Porous soft carbon	103 mAh g ⁻¹ at 0.5A g ⁻¹	No report	3000
12	Hard carbon	225 mAh g ⁻¹ at 0.05A g ⁻¹	No report	800
13	N-doped mesoporous carbon	240 mAh g ⁻¹ at 1A g ⁻¹	No report	70
14	Porous carbon	230 mAh g ⁻¹ at 0.02A g ⁻¹	No report	60
15	Bio-based carbon	112 mAh g ⁻¹ at 1A g ⁻¹	No report	1000

16	Carbon with expanded nanographite	150 mAh g ⁻¹ at 1A g ⁻¹	No report	1000
17	Pseudographite	355 mAh g ⁻¹ at 0.05A g ⁻¹	0.27 Ah cm ³	300
18	CNT/MoS ₂	450 mAh g ⁻¹ at 0.5A g ⁻¹	0.65 Ah cm ³	1000
19	Ti ₃ C ₂ MXene/CNT	200 mAh g ⁻¹ at 0.02A g ⁻¹	0.42 Ah cm ³	500

Supplementary References

1. Wen, Y. et al. (2014). Expanded graphite as superior anode for sodium-ion batteries. *Nat. Commun.* *5*, 4033.
2. Zhang, B., Ghimbeu, C.M., Laberty, C., Vix-Guterl, C. & Tarascon, J.-M. (2016). Correlation between microstructure and Na storage behavior in hard carbon. *Adv. Energy Mater.* *6*, 1501588.
3. Licht, S. et al. (2016). Carbon nanotubes produced from ambient carbon dioxide for environmentally sustainable lithium-ion and sodium-ion battery anodes. *ACS Cen. Sci.* *2*, 162-168.
4. Song, H., Li, N., Cui, H. & Wang, C. (2014). Enhanced storage capability and kinetic processes by pores- and hetero-atoms- riched carbon nanobubbles for lithium-ion and sodium-ion batteries anodes. *Nano Energy* *4*, 81-87.
5. Liu, Y. et al. (2014). In situ transmission electron microscopy study of electrochemical sodiation and potassiation of carbon nanofibers. *Nano Lett.* *14*, 3445-3452.
6. Cohn, A.P., Share, K., Carter, R., Oakes, L. & Pint, C.L. (2016). Ultrafast solvent-assisted sodium ion intercalation into highly crystalline few-layered graphene. *Nano Lett.* *16*, 543-548.
7. Cao, Y. et al. (2012). Sodium ion insertion in hollow carbon nanowires for battery applications. *Nano Lett.* *12*, 3783-3787.
8. Liu, H. et al. (2015). Nitrogen-rich mesoporous carbon as anode material for high-performance sodium-ion batteries. *ACS Appl. Mater. Interfaces* *7*, 27124-27130.
9. Li, Z. et al. (2016). High capacity of hard carbon anode in Na-ion batteries unlocked by POx doping. *ACS Energy Lett.* *1*, 395-401.
10. Sun, N., Liu, H. & Xu, B. (2015). Facile synthesis of high performance hard carbon anode materials for sodium ion batteries. *J. Mater. Chem. A* *3*, 20560-20566.
11. Cao, B. et al. (2016). Mesoporous soft carbon as an anode material for sodium ion batteries with superior rate and cycling performance. *J. Mater. Chem. A* *4*, 6472-6478.
12. Zhang, F. et al. (2017). High temperature carbonized grass as a high performance sodium ion battery anode. *ACS Appl. Mater. Interfaces*, *9*, 391-397.

13. Zhang, Y. et al. (2016). Lithium and sodium storage in highly ordered mesoporous nitrogen-doped carbons derived from honey. *J. Power Sources* *335*, 20-30.
14. Meng, X., Savage, P.E. & Deng, D. (2015). Trash to treasure: From harmful algal blooms to high-performance electrodes for sodium-ion batteries. *Environ. Sci. Technol.* *49*, 12543-12550.
15. Wu, L., Buchholz, D., Vaalma, C., Giffin, G.A. & Passerini, S. (2016). Apple-biowaste-derived hard carbon as a powerful anode material for Na-ion batteries. *ChemElectroChem* *3*, 292-298.
16. Yu, Z.-L. et al. (2016). Ion-catalyzed synthesis of microporous hard carbon embedded with expanded nanographite for enhanced lithium/sodium storage. *J. Amer. Chem. Soc.* *138*, 14915-14922.
17. Lotfabad, E.M. et al. (2014). High-density sodium and lithium ion battery anodes from banana peels. *ACS Nano* *8*, 7115-7129.
18. Liu, Y. et al. (2016). Liquid Phase Exfoliated MoS₂ nanosheets percolated with carbon nanotubes for high volumetric/areal capacity sodium-ion batteries. *ACS Nano* *10*, 8821-8828.
19. Xie, X. et al. (2016). Porous heterostructured MXene/carbon nanotube composite paper with high volumetric capacity for sodium-based energy storage devices. *Nano Energy* *26*, 513-523.